https://doi.org/10.1016/j.energy.2021.119920

Highlights

- The discontinuous S-shaped and the crescent ribs are introduced for a PEMFC flowing channel.
- Mass transfer, flow and energy performance of the PEMFC are described and evaluated.
- The enhancement of mass transport is much better than that of sinusoidal ribbed flow field.
- The proposed ribs improve the energy efficiency by up to 23.61% compared to a sinusoidal rib.

Credit Authorship Contribution Statement

The individual contribution of each author is as following:

Pengcheng DONG: Modeling and Simulation; Analysis; Writing original draft;

Gongnan XIE: Conceptualization; Analysis; Review and Editing draft; Supervision;

Meng NI: Method; Discussion and Analysis; Review and Editing draft.

Improved Energy Performance of a PEM Fuel Cell by Introducing Discontinuous S-shaped and Crescent Ribs into Flowing Channels

Pengcheng Dong [1], Gongnan Xie [1,*], Meng Ni [2]

[1] *School of Marine Science and Technology, Northwestern Polytechnical University, Xi'an, 710072, China.*

[2] *Department of Building and Real Estate, The Hong Kong Polytechnic University, Hong Kong, China.*

[*] Corresponding author, e-mail: xgn@nwpu.edu.cn (G. Xie).

Abstract

Better mass transfer, temperature distribution, pressure drop and the output performance could be achieved by realizing better flow field in PEM fuel cells. In the paper, based on the concept of a sinusoidal rib, two kinds of discontinuous ribs: S-shaped rib and crescent rib, are proposed and introduced into flowing channels of a PEM fuel cell. Results show that the presented ribs induce better flow field, and the local convection effect becomes stronger due to the velocity field changes, and that a better distribution of O_2 concentration benefits from the better flow pattern, resulting in an improvement of the electrochemical rate and an increase of the temperature. The pressure drop is effectively reduced and the electrochemical efficiency is improved by up to 23.61% in the condition of high current density, compared to those of the baseline sinusoidal ribbed flow field.

Keywords

PEM Fuel Cell; Discontinuous Ribs; Mass Transfer; Pressure drop; Performance Improvement.

Nomenclature

a	active surface area(1/m) / water activity
A	area(m^2)
C	concentration(mol/m^3)
C_r	condensation rate constant(mm)
d_r	the ribs thickness(mm)
D	diffusivity(m^2/s)
E	voltage(V) / potential(V)
EW	equivalent weight(kg/mol)
F	Faraday's constant(96485 C/mol)
H	height(mm)
i	exchange current density(A/m^2)
k	thermal conductivity(W/m·K)
K	permeability(m^2)
L	length (mm)
L_0	wavelength(mm)
L_r	the spacing of ribs(mm)
m	mass rate(kg/s)
M	molecular weight (kg/mol)
n	the number of electron
n_d	electro-osmotic drag coefficient
p	pressure(Pa)
R	universal gas constant(8.314 J/mol·K)
s	water saturation
T	temperature(K)
u	velocity vector(m/s)
V	voltages(V)
W	width(mm)
x	mass fraction

Greek symbols

α	the inlet/outlet angle / concentration dependence
γ	transfer coefficient
Γ	universal diffusivity(m^2/s)
ε	porosity
ζ	stoichiometric ratio
η	overpotential(V)
η_t	electrochemical efficiency
θ	angle
κ	the effective conductivity solid phase(S/m)
λ	water content
μ	viscosity (Pa·s)
ρ	density (kg/m^3)
σ	resistance($1/m^2$)/conductivity (S/m)
σ_T	standard deviation
ϕ	potential (V)
ϖ_T	uniformity index

Superscripts and Subscripts

a	anode
ACT	activation
c	cell /contact / capillary / cathode
cl	catalyst layer
CC	current collector
CH	channel
CON	concentration
d	dissolved water
eff	effective
EL	electrical energy
gdl	gas diffusion layer
l	liquid water
$loss$	potential loss
L	limited
$mass$	mass equation
mem	membrane
M	membrane
OHM	ohmic
OCV	open circuit voltage
p	proton
$pene$	hydrogen penetration
r	reversible
ref	reference
s	solid
sat	saturation
w	water saturation
wv	water vapor

1. INTRODUCTION

With the growth of the global population, existing fossil energy system cannot meet energy needs. As a large amount of fossil fuels are consumed, the level of CO_2 production increases in the industrial process, which is the main cause of the greenhouse effect. Renewable energy plays a key role in the transformation of the crisis. Hydrogen, the most abundant element in nature, can be obtained from fossil fuels such as coal, oil and natural gas. The energy content of hydrogen energy is exceed double of conventional foil fuels regardless of lower or higher heating value [1]. Electrochemical energy technologies are far superior to all heat engines in terms of thermodynamic efficiency [2]. It is well known than proton exchange membrane fuel cell (PEMFC) is an efficient and clean electrochemical power source. Its advantages are as follows: i) the only product of the electrochemical reaction is water, and the waste gas contains neither the toxic substances such Nitrides and Sulfides produced by conventional fuels nor greenhouse gases such as CO_2; ii) it is quieter and simpler than the internal combustion engine (ICE); iii) PEMFC operates at a lower temperature than other types of fuel cells, which providing the basic conditions for portable applications.

In fact, PEMFC is not very efficient in actual use. Its internal charge separation and ion transfer are limited by components and operating processes [3]: The reactants must be supplied through the flow channel and the porous electrode; Electrons and protons must be transmitted through macroscopic conductive medium to involve electrochemical reaction; Part of the reaction is the interface reaction, which has to overcome the activation energy; The product of the reaction can be converted to liquid, which impedes reactants and products transport. The above impediments to transmission and reaction lead to a decrease in efficiency.

In order to solve the problems faced by PEMFC, scholars have done a lot of research. A PEM fuel cell is generally composed of proton exchange membrane(PEM), catalyst(CL), gas diffusion layer(GDL) and current collector(CC) with flow field. Each of these parts great effects the efficiency of PEMFC. Huo et al. [4] investigated the water transfer behaviour on the catalyst layer and membrane based on cold start operating conditions. The transport characteristics of water and proton (H^+) in a swelling Nafion membrane and electro-osmosis were studied based on volumetric flux and flow potential measurements [5]. Proton travel modes in membrane is studied based on molecular dynamics [6]. Darcy et al. [7] analyzed the effect of thickness of Nafion films on oxygen permeability and proton resistivity at different temperature and relative humidity. About porous electrode (i.e. CL and GDL), its functions include: (1) Reaction gases and products transfer; (2) Ion and charge transport; (3) Desorption of the reactant at the reaction interface. In the CL, the life of material is a crucial factor affecting the PEMFC. However, the conditions conducive to the rapid participation of reactants in the chemical reaction will also lead to the dissolution of catalyst Pt in

the reduction reaction of oxygen and to the instability of the catalyst layer. To understand and improve the oxygen reduction reactions, the approaches of nanostructure and wettability enhancement at electrochemical reaction interfaces of the catalyst layer were summarized by Qiao et al. [8]. Meanwhile, a novel catalyst, such as SiO_2-Fe/N/C catalyst [9], was studied as an alternative to Pt. Different catalyst layer models have been studied to accurately predict cathode electrochemical reaction, among which agglomerate model [10, 11] has been most widely used and studied. To improve the transmission characteristics and pressure drop of the GDL, Hou et al. [12] considered the real GDL surface structure and proposed a 3D lattice Boltzmann model under the real GDL microstructure based on multi-component transmission. Polytetrafluoroethylene (PTFE) has an important effect on the hydrophobicity of diffusion layer. PTFE content and its effect on heat transfer performance have been studied and discussed [13]. In terms of numerical prediction, the thermal conductivity of the anisotropic GDL has been proved to improve the accuracy of mathematical modeling [14, 15].

For current collector, it plays a key role because the flow field ensures the distribution and transmission of the reactant gas. And the ribs on the CC determine the efficiency of conduction and heat transfer. According to the shaped and structure of ribs, the existing flow field structure can be divided into three types: continuous ribs flow field and discontinuous ribs flow field. (1) Common continuous ribs flow field: parallel, serpentine (single- and multi-channel), interdigitated [16], zig-zag and sinuous [17], leaf and lung inspired interdigitated design [18], and so on. Zigzag flow field has lower pressure and better water management than serpentine and interdigitated [17]. Sinusoidal flow field are proposed to change the dead zone of retention at the corners of zigzag flow field [19, 20]. It is found that the sinusoidal flow field significantly reduces the pressure drop, the higher velocity to drive water transfer, more uniform O2 distribution and better performance compared to the parallel flow field. (2) Discontinuous ribs flow field: mesh flow field, pin design [21], matrix flow field [22], honeycomb flow field [23], bionic design flow field [24], and so on. Wang et al. [21] and Atyabi et al. [22] found that conventional parallel flow field may led to insufficient gas supply when operating at high current densities, while serpentine flow field has large pressure drop. However, discontinuous ribs flow field can improve O_2 supply area and reduce pressure drop. At the same time, pin design flow field [21] and honeycomb flow field [23] also showed the lower pressure drop and the better flood relief. In addition, there are some flow field that are based on the combination of these two types flow fields.

Zigzag and sinusoidal have shown good heat transfer performance and low pressure drop characteristics in heat sink and printed circuit heat exchanger(PCHE). Wen et al. [25] studied the heat transfer and pressure drop characteristics of PCHE based on the sinusoidal and zigzag channel. The conclusion of PCHE's pressure drop characteristics is consistent with that of PEMFC. With the

requirement of miniaturization of electronic components, the S-shaped ribs obtained by discretization of sinusoidal ribs greatly improve the heat transfer performance and reduce the pressure drop. In heat sink, Nilpueng et al. [26] studied the discrete heat sink rib at a different phase angles and found that the discontinuous ribs had the best performance and pressure drop when the phase angle is equal to zero. S-shaped pressure drop was reduced by 1/7 compared with zigzag, while heat transfer performance [27]. In PCHE, the S-shaped structure can provide about 3.3 times less volume and lower pressure drop [28]. Alawadhi et al. [29] found that the S-shaped fin shape base on the cosine curve can eliminate the flow recirculation zones.

From the above literature, it can be obtained that discontinuous structure base on zigzag and sinusoidal design show the better thermal performance and pressure drop characteristics. Therefore, we will propose two different discontinuous ribs flow fields based on existing zigzag and sinusoidal to investigate pressure drop, mass transport and electrochemical characteristics of PEMFC. In the process of numerical modeling, the anisotropic material properties of the porous electrode are considered. The research of these two discontinuous ribs flow fields provides a novel idea for the study of flow field topology.

2. PHYSICAL MODELS AND RIBS DISCREET PROCESS

2.1 Continuous Ribs Discreet Process

In the paper, Fig.1 illustrates the design idea of the structure based on the sine flow field. For Fig.1 (*a*), sinusoidal ribs can be discretized at the different phase angles (the red line and the green line in Fig.1 (*a*) are $\pi/2$ apart in phase angles) to from different discrete structure. In the first discrete structure mode, the leading edge and trailing edge of each rib should be rounded to from a guide wing, because the guide wing can reduce pressure drop [27]. In the second discrete structure mode, the structure retains the sinusoidal curve of the inner edge while the outer edge is round. The sine curve based on the conventional zigzag design is shown is shown in Fig.1 (*b*). The bend angle, θ, is equal to 10° and the wavelength, L_0, is equal to $L/2$ (half of the length of the straight channel). The detailed parameters of the two novel discontinuous ribs flow field (Case B-A and B-S are the bionic discontinuous S-shaped ribs flow field, and Case C-A and C-S are the crescent ribs flow field) are shown in Fig.1 (*c*) (aligned, i.e., the same sine curve), where the rib thickness, d_r, is 1.0 mm and the spacing the ribs , L_r, is 2.0 mm.

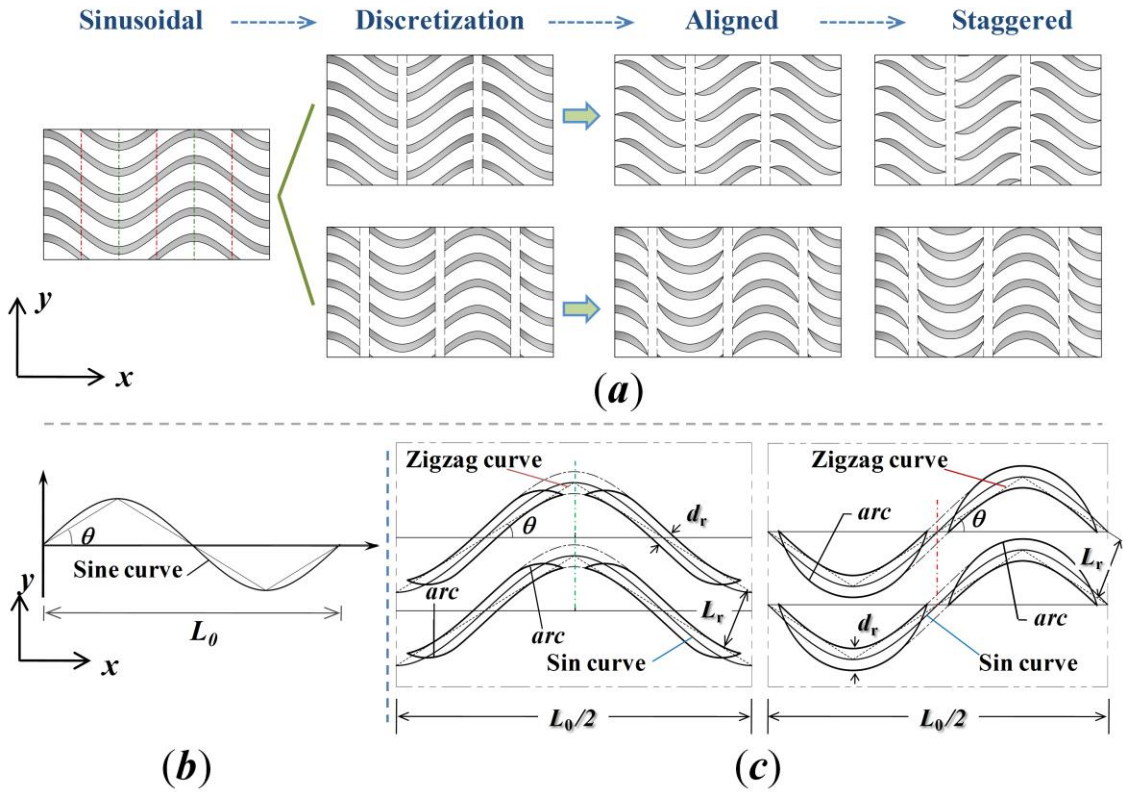

Fig.1 The conceptualization and the discrete method based on sine channel. (*a*) two different discrete process; (*b*) the reference curves in model design; (*c*) novel structure under two different discrete process.

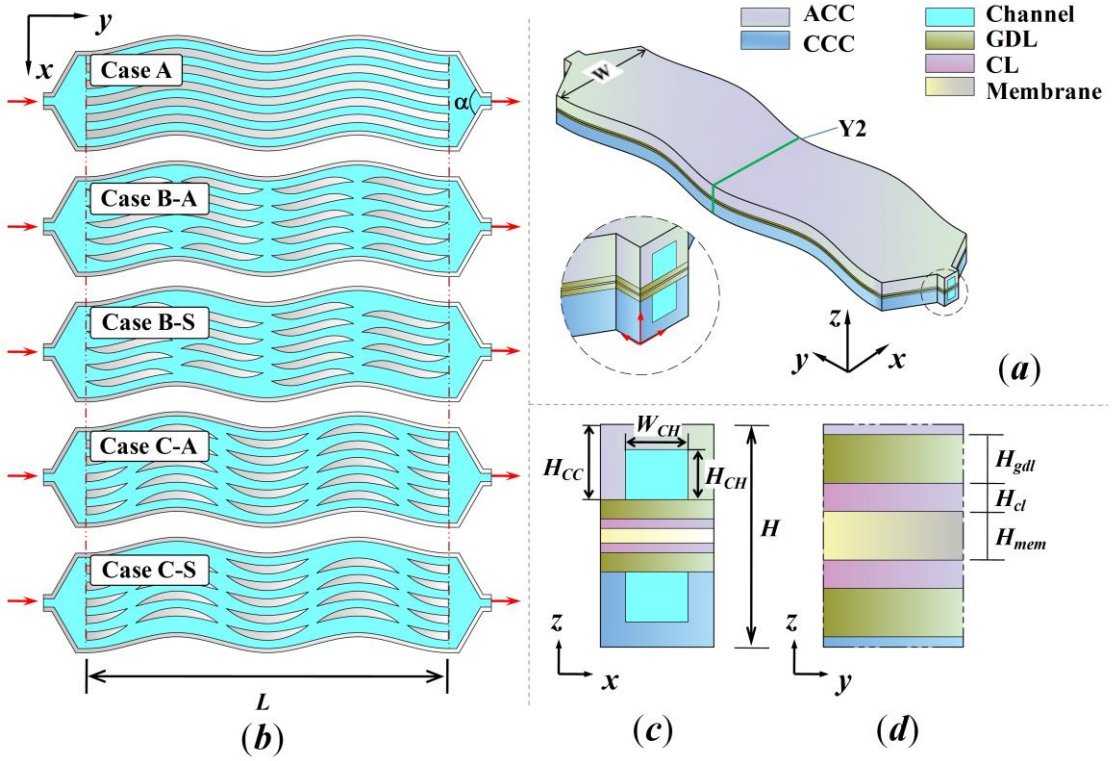

Fig.2 The structure diagram of the computational domain. (*a*) the component of PEMFC's computational domain; (*b*) the sinus channels (Case A, continuous ribs), the discontinuous S-shaped (Case B-A and B-S) and the crescent (Case C-A and C-S) ribs channel; (*c*) the global parameter of computational domain; (*d*) the global parameter of porous electrode and membrane.

2.2 Computational Domain

As shown in Fig.2, the 3D multi-layer computational domain, consisting of anode current collector (ACC), cathode current collector (CCC), gas diffusion layer (GDL), catalyst layer (CL), channel and membrane, is established. It can be seen from Fig.1 that two discrete modes will produce different structure. Therefore, sinusoidal flow field will be used as the basic reference case –– Case A, and two structures are discussed under the layout of aligned and staggered as shown in Fig.2 (*b*) (i.e., Case B-A, Case B-S, Case C-A and Case C-S). The inlet and outlet angle of the flow field is set at 120°. And the ratio, W_{CH} : H_{CH}, is equal to 1.0. The height of the entire computational domain (H) is equal to 3.47 mm (i.e., H=2H_{CC} + 2H_{gdl} + 2H_{cl} + H_{mem}). Other model parameters and operating conditions are listed in Table 1.

3. DETAILS OF NUMERICAL SIMULATIONS

3.1 Overview

In this paper, the finite volume method (FVM) is used to investigate the output performance and flow characteristics of two novel discontinuous ribs flow fields under different layouts. The 2016 version of SOLIDWORKS is adopted for the construction of geometric models. In the preprocessing, the grids are composed of hexahedral and tetrahedral meshes (structured and unstructured meshes), and are generated by ICEM. The governing equation and electrochemical dynamic process was solved by FLUENT version 15.0 based on the FVM.

3.2 Assumptions

PEMFC is a complex multi-physical system, including flow, energy, species transfer and transmission, electrochemistry and porous media. It is very difficult to solve the complex physical model. Therefore, the hypothesis is presented.

1) The ideal gas equation of state is applied.
2) The reactants are incompressible.
3) Flow is solved based on steady state and laminar flow (Re<500).
4) The heat conduction of porous materials satisfies isotropy (CL and membrane) and anisotropy (GDL).
5) The electrochemical rate of the electrode is described using the Butler-Volmer equation and the contact resistance between the layers is ignored.

3.3 Electrochemical Reaction Equation and Governing Equations

3.3.1 Electrode electrochemical reaction [30]:

When the PEM fuel cell starts to work, the fuel (H_2) and the oxidant (O_2 or air) enter the cell from inlet of CC at the anode and cathode respectively. The hydrogen diffuses through the porous media to the CL on the anode side. Hydrogen arrives involves in electrode chemical reaction at the

three-phase boundary (TPB) of the CL (i.e., the interface between gas, liquid and solid) as shown in Eq. (1). Hydrogen is desorbed in the presence of a catalyst to form protons (H^+) and electrons (e^-) (Oxidation Reaction). The protons pass through the hydrated proton exchange membrane and reach the CL on the cathode. And electrons travel through the anode conductor (ACL, AGDL and ACC), the external circuit connected with the load, and the cathode conductor to reach the CL at the cathode side. Similarly, oxygen diffuses to the CCL. Another electrode reaction will be performed based on oxygen, protons and electrons on the cathode TPB (Reduction Reaction), as shown in Eq. (2). The overall reaction of the PEMFC is similar to the combustion reaction, as shown in Eq. (3).

$$H_2 \rightarrow 2H^+ + 2e^- \tag{1}$$

$$\frac{1}{2}O_2 + 2H^+ + 2e^- \rightarrow H_2O \tag{2}$$

$$H_2 + \frac{1}{2}O_2 \rightarrow H_2O + heat \tag{3}$$

3.3.2 Conservation equations

As a physical system coupled with multiphysics process, the conservation equations involved in mathematical model of PEMFC include: mass conservation, momentum conservation, energy conservation, species conservation and charge conservation. The general form of these conservation equations is shown below.

$$\frac{\partial(\rho \boldsymbol{\Phi})}{\partial t} + \nabla \cdot (\rho \vec{u} \boldsymbol{\Phi}) = \nabla \cdot (\boldsymbol{\Gamma}_{\boldsymbol{\Phi}} \nabla \boldsymbol{\Phi}) + S_{\boldsymbol{\Phi}} \tag{4}$$

where ρ is the density, $\boldsymbol{\Phi}$ is the variable to be solved, t and $\vec{u}$ are the time and the velocity vector, respectively. $\boldsymbol{\Gamma}_{\boldsymbol{\Phi}}$ is the universal diffusivity and $S_{\boldsymbol{\Phi}}$ is the (universal) source term. It is worth noting that the four terms in Eq. (4), from left to right, are the unsteady term, the convection term, the diffusion term and the source term, respectively.

If $\boldsymbol{\Phi}$= 1, Eq. (4) represents the equation of continuity [31]:

$$\frac{\partial \rho}{\partial t} + \nabla \cdot (\rho \vec{u}) = S_{mass} \tag{5}$$

If $\boldsymbol{\Phi}$= $\vec{u}$, Eq. (4) represents the momentum conservation equation [31]:

$$\frac{\partial(\rho \vec{u})}{\partial t} + \nabla \cdot (\rho \vec{u} \vec{u}) = \nabla \cdot (\mu \nabla \vec{u}) + S_{\vec{u}} \tag{6}$$

the source term $S_{\vec{u}}$ is the momentum loss of the fluid in the porous electrode (i.e., CL and GDL). Darcy's law is applied to CL and GDL, and the expression of source term is as follows:

$$S_{\vec{u}} = -\frac{\mu}{K}\vec{u} \tag{7}$$

where μ is dynamic viscosity of the fluid and K is the permeability of the porous layer.

If $\boldsymbol{\Phi}= T$, Eq. (4) represents the momentum conservation equation [31]:

$$\frac{\partial(\rho T)}{\partial t}+\nabla\cdot(\rho\vec{u}T)=\nabla\cdot\left(\frac{k_{eff}}{c_p}\nabla T\right)+S_T \tag{8}$$

where c_p and k_{eff} are the specific heat at constant pressure and effective thermal conductivity, respectively. S_T is the source term of energy conservation equation, i.e., the rate of heat production caused by the electrochemical reaction.

$$S_T=\left(\frac{\vec{i}_e^{\,2}}{k_e^{eff}}+\frac{\vec{i}_s^{\,2}}{\sigma_s^{eff}}\right)+j\left(\eta+T\frac{dU_0}{dT}\right)+h_L \tag{9}$$

The first term, $\left(\frac{\vec{i}_e^{\,2}}{k_e^{eff}}+\frac{\vec{i}_s^{\,2}}{\sigma_s^{eff}}\right)$, is the heating generation due to the ohmic resistance; σ_s^{eff} and k_e^{eff} are the electron resistance and proton resistance, respectively. $j\left(\eta+T\frac{dU_0}{dT}\right)$ is the generate heat due to the electrochemical reaction at the CL; η is activation overpotential and $j=\frac{d\vec{i}_e}{dy}$. And h_L is the change in heat caused by a phase-transition.

If $\boldsymbol{\Phi}= Y_i$, Eq. (4) represents the species conservation equation [31]:

$$\frac{\partial(\rho Y_i)}{\partial t}+\nabla\cdot(\rho\vec{u}Y_i)=\nabla\cdot\left(D_i^{eff}\nabla Y_i\right)+S_{Y_i} \tag{10}$$

where Y_i *and* S_{Y_i} are the mass fraction and the species source term (the rate of consumption or production of reactant species at CL) of species i (i.e., H_2, O_2 and H_2O). and D_i^{eff} is the effective diffusivity of the ith species. That is

$$D_i^{eff}=\varepsilon^{1.5}D_i \tag{11}$$

$$D_i=\varepsilon^{1.5}(1-\mathrm{s})^{2.5}D_i^0\left(\frac{p_0}{p}\right)\left(\frac{T}{T_0}\right)^{1.5} \tag{12}$$

D_i, ε *and* s denote the mass diffusivity of species ith, the porous electrode and water saturation, respectively. And D_i^0 is the reference mass diffusivity of species ith based on the standard condition (p_0, T_0).

If $\boldsymbol{\Phi}=\phi_p$ *or* ϕ_e (the potential of the proton or electron), Eq. (4) represents the charge conservation equation [31]:

$$\begin{cases}0=\nabla\cdot\left(\sigma_p\nabla\phi_p\right)+S_{\phi_p}\\ 0=\nabla\cdot\left(\kappa_e\nabla\phi_e\right)+S_{\phi_e}\end{cases} \tag{13}$$

It is note that the transient term can be ignored the electrochemical reaction time is very short compared with the fluid flow. σ_p and κ_e denote the effective conductivity of proton (PEM) and electron (solid phase), respectively. And S_ϕ is the source term. The electrolyte phase's conductivity is modeled as Eq. (14) and is the function of water content λ and temperature T.

$$\sigma_p = (0.514\lambda - 0.326)e^{1268\left(\frac{1}{303}-\frac{1}{T}\right)} \tag{14}$$

The source terms based on the conservation equations are summarized in Table 2. The modeling physical parameters and material characteristic parameters used in the mathematical modeling refer to Ref. [30,31] are listed in Table 3.

3.3.3 Electrochemical modeling and electrochemical reaction rate

The chemical reaction of PEMFC is similar to the combustion reaction of H_2, that is, exothermic reaction. The change in chemical energy can be expressed in terms of the variation of Gibbs free energy (ΔG), as shown below.

$$\Delta G = \Delta H - T\Delta S \tag{15}$$

where ΔH *and* ΔS are the change in the enthalpy of electrochemical reaction and the variation of entropy. According to chemical thermodynamics, it can be known that:

$$\Delta G = -nFE_r \tag{15}$$

n, F and E_r denote the number of electron moles exchange per mole of hydrogen, Faraday's constant and the reversible voltage ($E_r \approx 1.23$V). Usually, pressure change have an effect on the reversible voltage [32], the corrected voltage can be obtained:

$$E_r = -\frac{\Delta G}{nF} - \frac{RT}{2F}\ln\frac{p_{H_2O}}{p_{H_2}p_{O_2}} \tag{16}$$

In practice, PEMFC usually has an open circuit voltage (E_{OCV}) of less than 1.0 V due to potential loss because of hydrogen penetration and internal current [33].

$$E_{OCV} = E_r - \frac{RT}{nF}\ln\left(\frac{i_{pene}+i_{loss}}{i}\right) \tag{17}$$

where i is the exchange current density.

Different electrochemical reactions in the CL on the anode and cathode, which lead to the consumption and the release of electrons. In order to establish the relationship between current and potential, the kinetic equation of electron process (Butler-Volmer equation) was applied.

$$i_a = \left(i_a^{ref}a\right)\left(\frac{C_a}{C_a^{ref}}\right)^{\gamma_a}\left(e^{\alpha_a F\eta_a/RT} - e^{-\alpha_c F\eta_a/RT}\right) \tag{18}$$

$$i_c = \left(i_c^{ref} a\right)\left(\frac{C_c}{C_c^{ref}}\right)^{\gamma_c}\left(-e^{\alpha_a F\eta_c/RT} + e^{-\alpha_c F\eta_c/RT}\right) \tag{19}$$

where i^{ref} and a are the reference exchange current density per active surface area and the reaction area of CL, respectively. C and C^{ref} denoted the local species concentration and the reference concentration. α and γ is the transfer coefficient and concentration dependence. η_a and η_c are the driving forces for electron process and also the local surface over-potential (the activation loss) in anode and cathode. It is usually defined by the potential difference between the solid phase and the electrolyte.

$$\eta_a = \phi_e - \phi_p \tag{23}$$

$$\eta_c = \phi_e - \phi_p - E_{OCV} \tag{24}$$

where ϕ_p and ϕ_e are the potential of solid phase and electrolyte phase, respectively. The E_{OCV} term is the open-circuit voltage (OCV).

3.3.4 *I-V* curve and efficiency

The operating voltage for PEMFC is usually lower than the OCV due to the inevitable loss of ohmic polarization, activation energy and concentration polarization of the cell itself.

$$V_c = E_{OCV} - V_{OHM} - V_{ACT} - V_{CON} \tag{25}$$

here, V_{OHM}, V_{ACT} and V_{CON} are the ohmic voltages, the activation voltages and the concentration voltages, respectively. These three terms can be calculated from Eq. (13), Eqs. (18-19) and Eq. (26) [34].

$$V_{CON} = \frac{RT}{nF}\ln\left(\frac{i_L}{i_L - i}\right) \tag{26}$$

where, i and i_L are the current density and the limiting current density, respectively.

Efficiency is defined as the ratio of effective output energy to input energy. For PEMFC, the output energy is electrical energy and the input energy is consumed hydrogen.

$$\eta_t = \frac{W_{EL}}{W_{H_2}} = \frac{V_c}{\Delta H/nF} \tag{27}$$

for hydrogen, ΔH = 286 kJ/mol at the higher heating value (HHV) and ΔH = 241 kJ/mol at the lower heating value (LHV). LHV efficiency will be used in the paper, as shown below.

$$\eta_t = \frac{V_c}{1.254} \tag{28}$$

3.3.5 Liquid water formation and transport equation

PEMFC usually operates at the relatively low temperatures that will result in the conversion of water vapor to liquid water. Proton exchange membrane can be hydrated by liquid water, which provides a good foundation for protons (H^+) transport. However, liquid water will prevent the gas

from reaching the TPB and thus reduce the reaction efficiency and PEMFC's performance. The prediction of liquid water can be established by the water saturation, *s*, to model the formation and transport [35].

$$\frac{\partial(\varepsilon\rho_l s)}{\partial t}+\nabla\cdot\left(\rho_l\frac{Ks^3}{\mu_l}\frac{dp_c}{ds}\nabla s\right)=S_w \tag{29}$$

where ρ_l and μ_l are the density and viscosity coefficient of liquid saturation. And ε is the porosity. p_c, the capillary pressure of porous media, is the function of saturation. It can be defined by Eq. (32). Note that S_w is the source term of saturation.

$$S_w=\begin{cases}(1-s)C_r\dfrac{p_{wv}-p_{sat}}{RT}M_{H_2O} & p_{wv}>p_{sat}\\ sC_r\dfrac{p_{wv}-p_{sat}}{RT}M_{H_2O} & p_{wv}<p_{sat}\end{cases} \tag{30}$$

The source term is only used in the CL and GDL and applied to the phase change at the cathode side only. And C_r is the condensation rare constant is defined by C_r=100s^{-1}. p_{wv} and p_{sat} are the water vapor pressure and the saturation pressure respectively. The p_{sat} is modeled as,

$$\begin{aligned}\log_{10}p_{sat}=&-2.1794+0.02953(T-273.15)\\&-9.1837\times10^{-5}(T-273.15)^2+1.4454\times10^{-7}(T-273.15)^3\end{aligned} \tag{31}$$

$$p_c=\begin{cases}\sigma\cos\theta_c\sqrt{\dfrac{\varepsilon}{K}}\left(1.41(1-s)-2.12(1-s)^2+1.263(1-s)^3\right) & \theta_c<90^\circ\\ \sigma\cos\theta_c\sqrt{\dfrac{\varepsilon}{K}}\left(1.41s-2.12s^2+1.263s^3\right) & \theta_c>90^\circ\end{cases} \tag{32}$$

here σ and θ_c are the surface tension and the contact angle, respectively. *K* is the permeability.

For the channel, Eq. (29) can be simplified for Eq. (23), that is:

$$\frac{\partial(\rho_l s)}{\partial t}+\nabla\cdot(\rho_l\vec{v}_l s)=\nabla\cdot(\Gamma_l\nabla s) \tag{33}$$

where Γ_l and $\vec{v}_l$ are the diffusion coefficient and the velocity of liquid water in channel. The term, $\vec{v}_l$, is equal to the gas velocity (i.e., the mist).

3.3.6 Water transport in membrane [35]

For the swelling membrane, water can percolate in proton exchange membrane due to migration (electro-osmotic drag) and diffusion (the gradient of concentration and pressure). In PEM, the water molecules tend to agglomerate locally under the action of hydrogen bonds to form water molecular clusters. Therefore, water is usually assumed to be "the dissolved phase". Eq. (34) describes the water transport in the membrane.

$$\frac{\partial(\varepsilon C_d)}{\partial t}+\nabla\cdot(-\Gamma_d\nabla C_d)+\nabla\cdot\left(\frac{n_d}{F}\vec{i}_p\right)=S_d \tag{34}$$

where C_d is the dissolved water concentration. Γ_d is the diffusivity of water content. n_d is the electro-osmotic drag coefficient. And $\vec{i}_p$ is the membrane phase current density (i.e., $\vec{i}_p = \sigma_p \nabla \phi_p$). S_d is the water generation rate at the cathode TPB due to the electrochemical reaction (i.e., the volumetric source term S_{H_2O}).

$$C_d = \frac{\rho_w M_w \lambda}{EW} \tag{35}$$

$$n_d = \frac{2.5\lambda}{22} \tag{36}$$

$$\Gamma_d = f(\lambda) e^{2416\left(\frac{1}{303} - \frac{1}{T}\right)} \tag{37}$$

where, ρ_w and EW are the dry membrane density and the equivalent weight of the membrane respectively. And $f(\lambda)$ can be computed form Eq. (38):

$$f(\lambda) = \begin{cases} 3.10\times10^{-7}\lambda\left(e^{0.28\lambda}-1\right)e^{-2346/T} & 0<\lambda<3 \\ 4.17\times10^{-8}\lambda\left(1+161e^{-\lambda}\right)e^{-2346/T} & other \end{cases} \tag{38}$$

The water content, λ, is the number of water molecules per sulfonic group. It can be obtained by:

$$\lambda = \begin{cases} 0.043+17.18a-39.85a^2+36a^3 & a<1.0 \\ 14+1.4\left(a-1\right) & a>1.0 \end{cases} \tag{39}$$

here a stand for the water activity that is calculated by the vapor molar fraction and the local pressure,

$$a = \frac{x_{H_2O} p}{p_{sat}} + 2s \tag{40}$$

3.4 Boundary Conditions and Solution Method

For the inlet and outlet, Dirichlet and Neumann boundary condition [36] are applied respectively. The mass rate, temperature and species mass fraction are specified and the water saturation is zero at the inlet. The mass rate of anode and cathode is defined by Eq. (41) and (42), respectively. The stoichiometric ratio, ζ, are given in Table 1. For the outlet, the pressure boundary condition is used.

$$\dot{m}_a \geq \frac{\zeta_{H_2}}{x_{H_2}} \frac{M_{H_2}}{2F} i_a^{ref} A_M \tag{41}$$

$$\dot{m}_c \geq \frac{\zeta_{O_2}}{x_{O_2}} \frac{M_{O_2}}{4F} i_a^{ref} A_M \tag{42}$$

At the other external boundary (terminal of PEMFC), temperature and potential are specified. The electron potential, ϕ_e =0 and ϕ_e =V_{cell} , are applied by the terminal of anode and cathode, respectively. And Neumann boundary condition is used to the potential field boundary and zero flux boundary inside the PEMFC.

The SIMPLE algorithm is adopted to the governing equation, and F-Cycle is selected for all equation. The pressure term choose the standard format and the other term can adopt to the first-order upwind schemes at the before stable convergence. The second-order upwind schemes will apply to improve the calculation accuracy.

3.5 Grid Independence

In order to improve the efficiency of calculation and ensure the accuracy of simulation result, the sinusoidal flow field (Case A) is selected as the baseline to do the grid independence under the different grid systems. In the paper, the mesh pattern of tetrahedral and hexahedral meshes (i.e. unstructured and structured meshes) are adopted. Hexahedral meshes were used in CL and membrane and the tetrahedral meshes were applied in other parts. The global grid of computational domain and the grid near the flow channel are shown in Fig. 3. The three grid systems are: 2.41M, 3.43M and 5.03M, respectively. The mass fraction of oxygen at the intersection line between Y2 and interface of CL and GDL is used as the variable, as shown in Fig. 4. The grid system of 5.03M are the baseline. The errors of the first two grid systems are 1.31% (2.41M) and 0.48% (3.43M), respectively. Therefore, the grid system of about 3.34M was selected to finish the other analysis and calculation considering the calculation accuracy and the workload comprehensively.

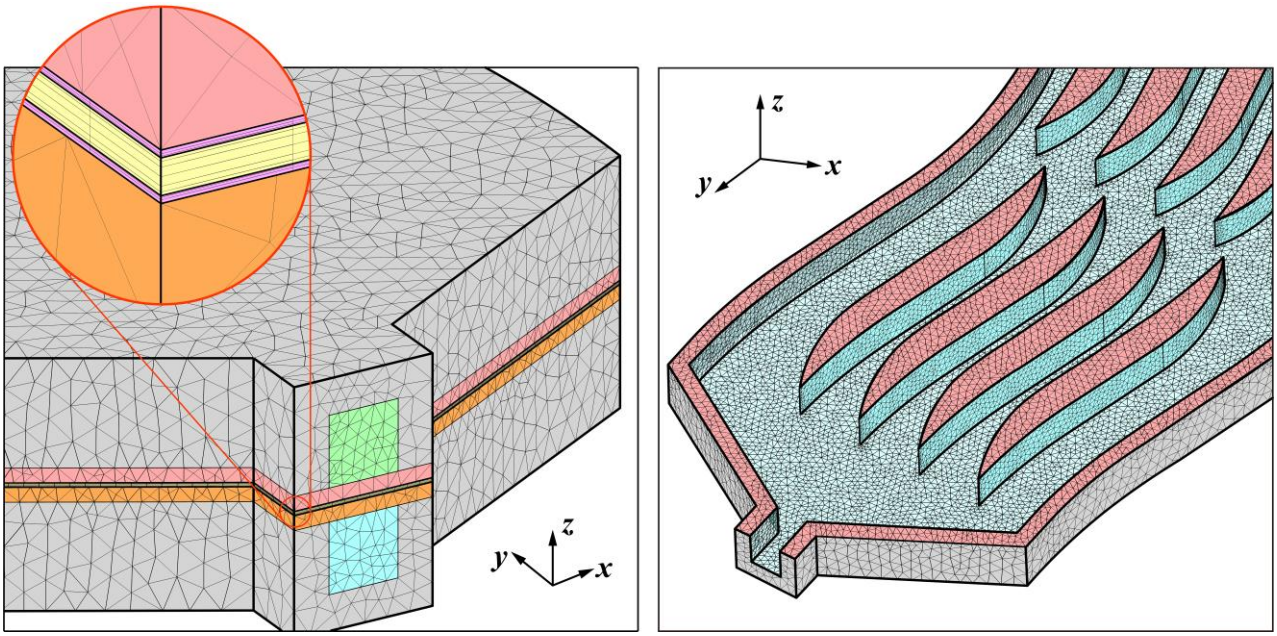

(*a*) **(*b*)**

Fig.3 The mixed grid based on unstructured and structured mesh (take Case B-S as an example). (*a*) the 3D global grid diagram; (*b*) the local grid near the channel.

3.6 Model Validation

In order to verify the correctness of the numerical calculation, the simulation results were compared with the known experimental results of Wang et al. [37] based on the same operating conditions (T=353.15 K, p=3.0 atm), as shown in Fig. 5. In the numerical models verification, the same model as the experiment is used – the current collector with a serpentine flow field. The simulation results are in good agreement with the experimental results.

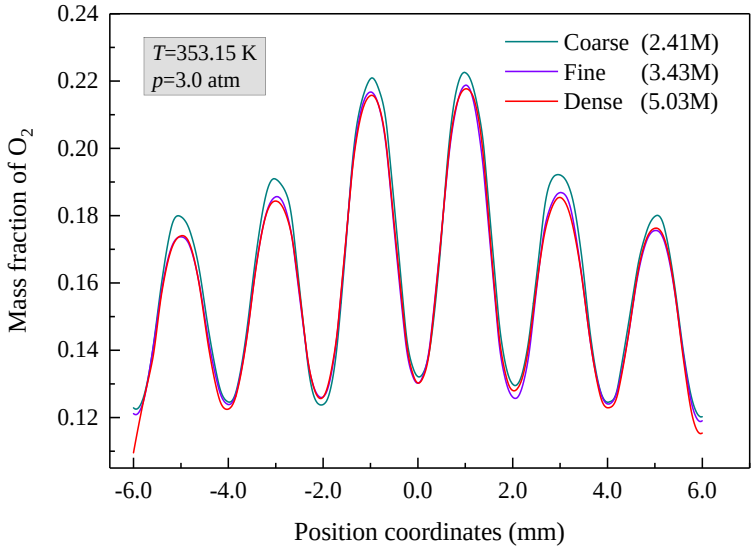

Fig.4 The mass fraction of O_2 for the intersection of Y2 and the interface membrane and catalyst on cathode based on the different grid systems at 0.3V (the intersection line: z=0.0 mm).

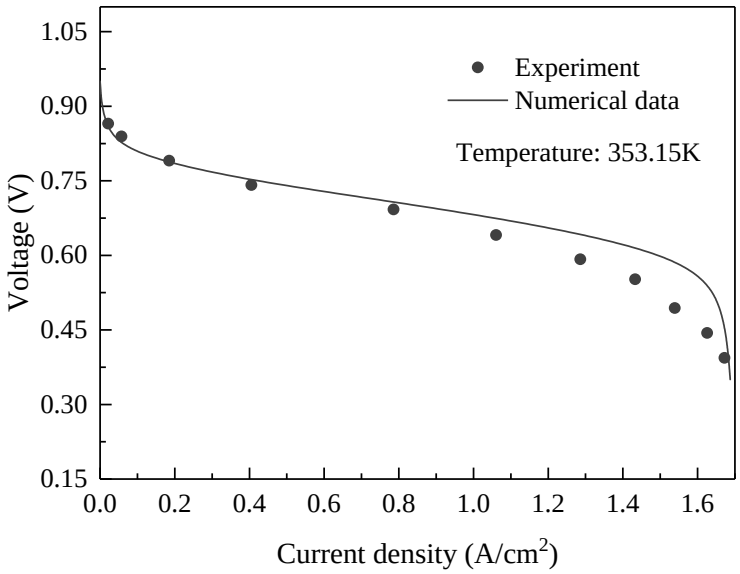

Fig.5 The error comparison between the simulation result and the experiment data (Wang et al. [37]).

4. RESULTS AND DISCUSSION

4.1 The output performance of PEMFC

The polarization curve can directly reflect the PEMFC's performance and is widely applied. The PEMFC's performance curves of several different structure in the paper are shown in Fig. 6.

Fig. 6 (a) shows the relationship between operating voltage and the PEMFC's current density, and Fig. 6 (b) shows the variation of the power density during the working progress. It can be found that the performance of the two proposed novel flow fields is better than the sinusoidal flow field (Case A). Generally, the power density first gradually increases and then decreases and the maximum power density is around 0.9 W/cm^2. In the higher current density area, the power density of two novel structure from high to low is Case B-S, Case C-A, Case B-A, Case C-S and Case A, respectively. However, the performance of PEMFC is similar in the low current density area. Higher power density means smaller size of PEMFC, which is important for PEMFC miniaturization. The performance improvement of Case B-S, Case C-A and Case B-A are obviously greater than Case C-S. Flow, mass transfer and temperature will be further discussed based on 0.4V in the following.

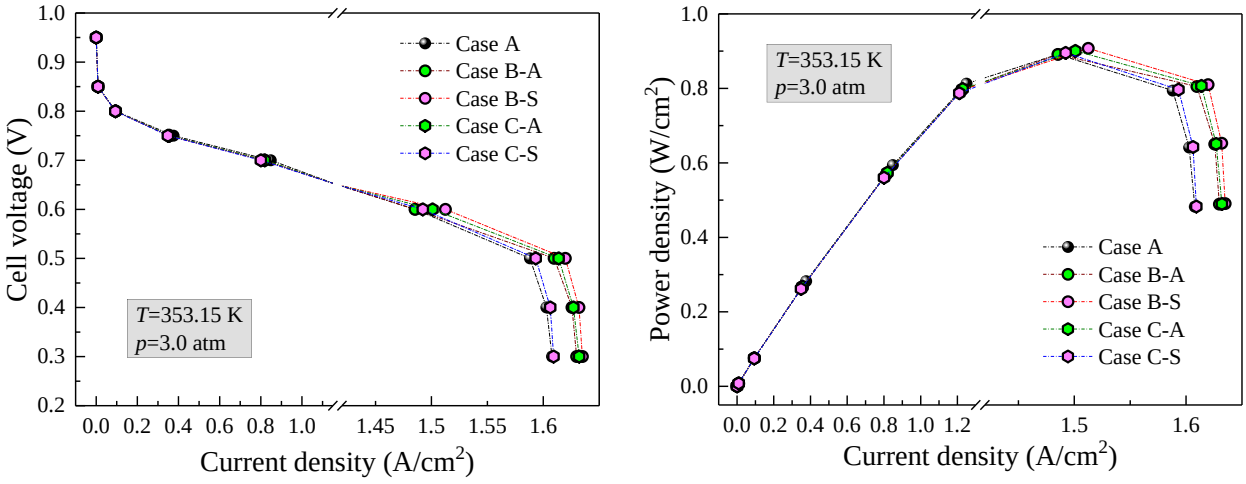

Fig.6 The polarization curve and power curve of the different cases. (*a*) PEMFC's operating voltage; (*b*) the relationship between the power density and current density.

4.2 The flow characteristics in flow field

There are three methods of mass transfer in PEM fuel cell: electromigration, convection and diffusion. The flow state of reactants and products in the flow field obviously effects the species transfer process, which leads to the change of electrochemical reaction rate of PEM fuel cell. The streamline of the flow field and the velocity of *y*-direction at the cathode side are shown in Fig. 7. It can be seen from Fig. 7 that the flow pattern of the discontinuous S-shaped ribs flow field (Case B-A and Case B-S) and the crescent ribs flow field (Case C-A and Case C-S) is different compared to the sinusoidal flow field (Case A). Case B-A and Case B-S are greater than other cases for the flow velocity along the *y* direction. Besides, the leading edge and trailing edge of two novel structure can guide the fluid flow, which improve the flow state as can be seen from the streamline in Fig. 7.

As the sinusoidal flow field is discrete at different phase angle, the flow state of the fluid in the novel discontinuous ribs flow field can be changed, which leads to the change of pressure drop and velocity, and the mass transfer state will be affected. For adjacent discontinuous ribs, the fluid

velocity decreases near the trailing edge in front due to the divergent structure and then increases at the leading edge due to the convergent structure, which facilitates the water transport. For Case B-A and Case B-S, the discrete position appears at the limit point where the flow direction turns. But the discrete position for Case C-A and Case C-S come into being along the path of fluid. Compared with zigzag flow channel, the improvement of sinusoidal flow field performance lies in the change of the stagnation zone at the turning point of flow in the zigzag flow channel. However, the sinusoidal flow field is likely to appear a low-speed retention area on the inside of the turning point of flow direction, which can generate water retention. Case B-A and Case B-S can weaken the effect but water retention can appear in the same place. On the contrary, the discrete position of Case C-A and Case C-S are applied to the stagnation zone, which will increase the velocity of position and improve the flow field. Therefore, the velocity distribution along *y*-direction of Case B-A and Case B-S is superior to Case C-A and Case C-S.

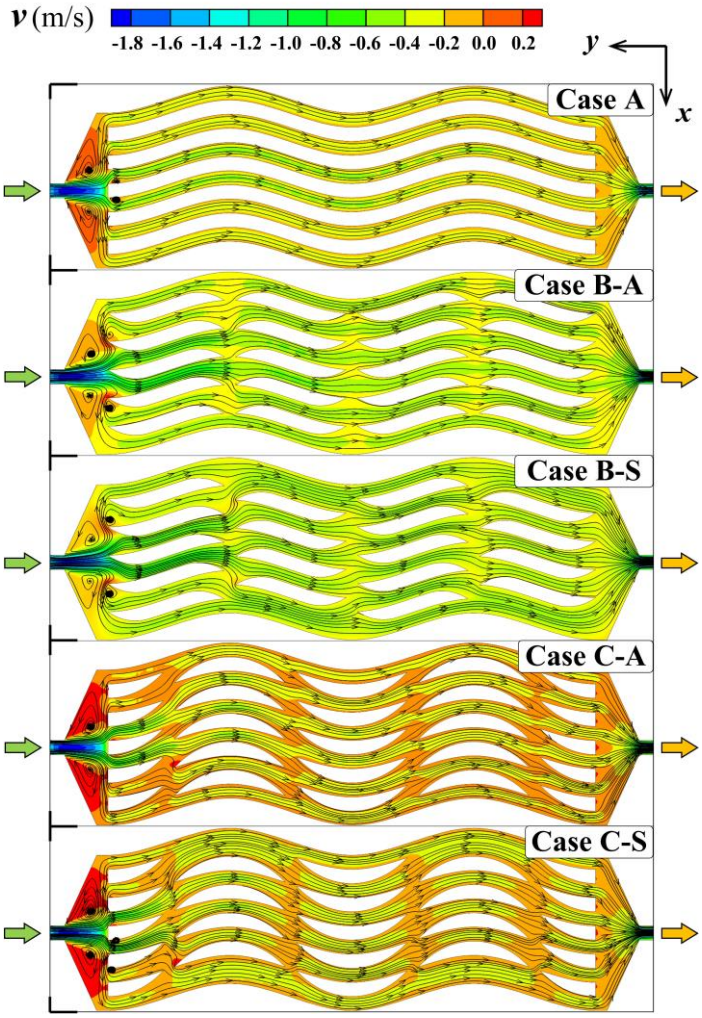

Fig.7 The streamline and velocity in the *y*-direction on the middle surface of the flow field on cathode at the 0.4V

4.3 Temperature uniformity and local temperature distribution

As an important factor affecting PEMFC's performance, the proton transport and electrochemical rate depend on it on the on hand, and the durability and the thermal stress of

materials on the other hand. In order to evaluate the uniformity of temperature distribution for the membrane, the temperature standard deviation, σ_T, and uniformity index, ϖ_T, on the neutral plane along *z*-direction of the membrane were used. σ_T and ϖ_T are defined as follows.

$$\sigma_T = \left(\frac{\sum \left(T_i - \bar{T} \right)^2}{N} \right)^{1/2} \tag{43}$$

where T_i is the temperature at each of the N selected points. And $\bar{T}$ is the arithmetic mean of the N selected points, $\bar{T} = \sum T_i / N$.

$$\varpi_T = 1 - \frac{\sum \left[\left| T_i - \bar{T}_A \right| A_i \right]}{2 \left| \bar{T}_A \right| \sum A_i} \tag{44}$$

where A_i is the facet area in the neutral plane. And $\bar{T}_A$ is the weighted average of the area, as shown below.

$$\bar{T}_A = \frac{\sum T_i A_i}{\sum A_i} \tag{45}$$

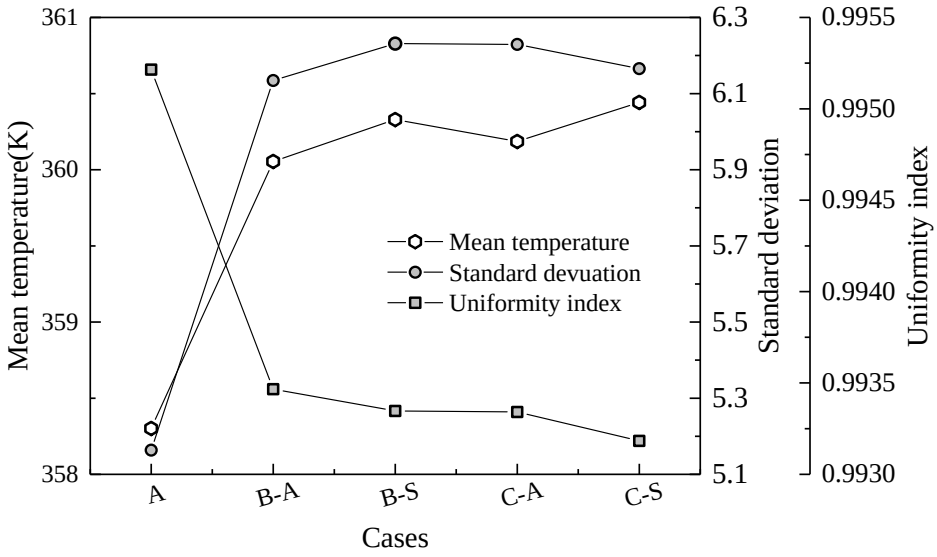

Fig.8 The characterization of mean temperature and temperature uniformity on the mid plane of membrane at 0.4V

The average temperature and temperature uniformity of the neutral plane of the membrane are shown in Fig. 8. It can be seen that the mean temperature of novel structure is greater than the sinusoidal flow field (Case B-A, Case B-S, Case C-A and Case C-S larger than Case A). And it is worth noting that Case B-S has the largest increment. More heat is generated as a result of an increase in the rate of chemical reaction. From a statistical point of view, the standard deviation illustrate the degree to which each sample point deviates from the mean. The deviation of the novel structure based on σ_T is larger than the sinusoidal flow field (Case A), which indicates that the deviation degree of the mean temperature is higher. The temperature uniformity index, ϖ_T, from

high to low is: Case A > Case B-A > Case B-S > Case C-A > Case C-S. This mean that the uniformity of temperature distribution decreases gradually. The decreasing amplitude of ϖ_T is in turn: 0.175% (Case B-A), 0.187% (Case B-S), 0.188% (Case C-A), 0.204% (Case C-S), respectively. Although the temperature uniformity index, ϖ_T, of the novel structure is smaller than of Case A, its decline is very small (the maximum value is 0.204%). Therefore, the distribution of the global temperature is acceptable.

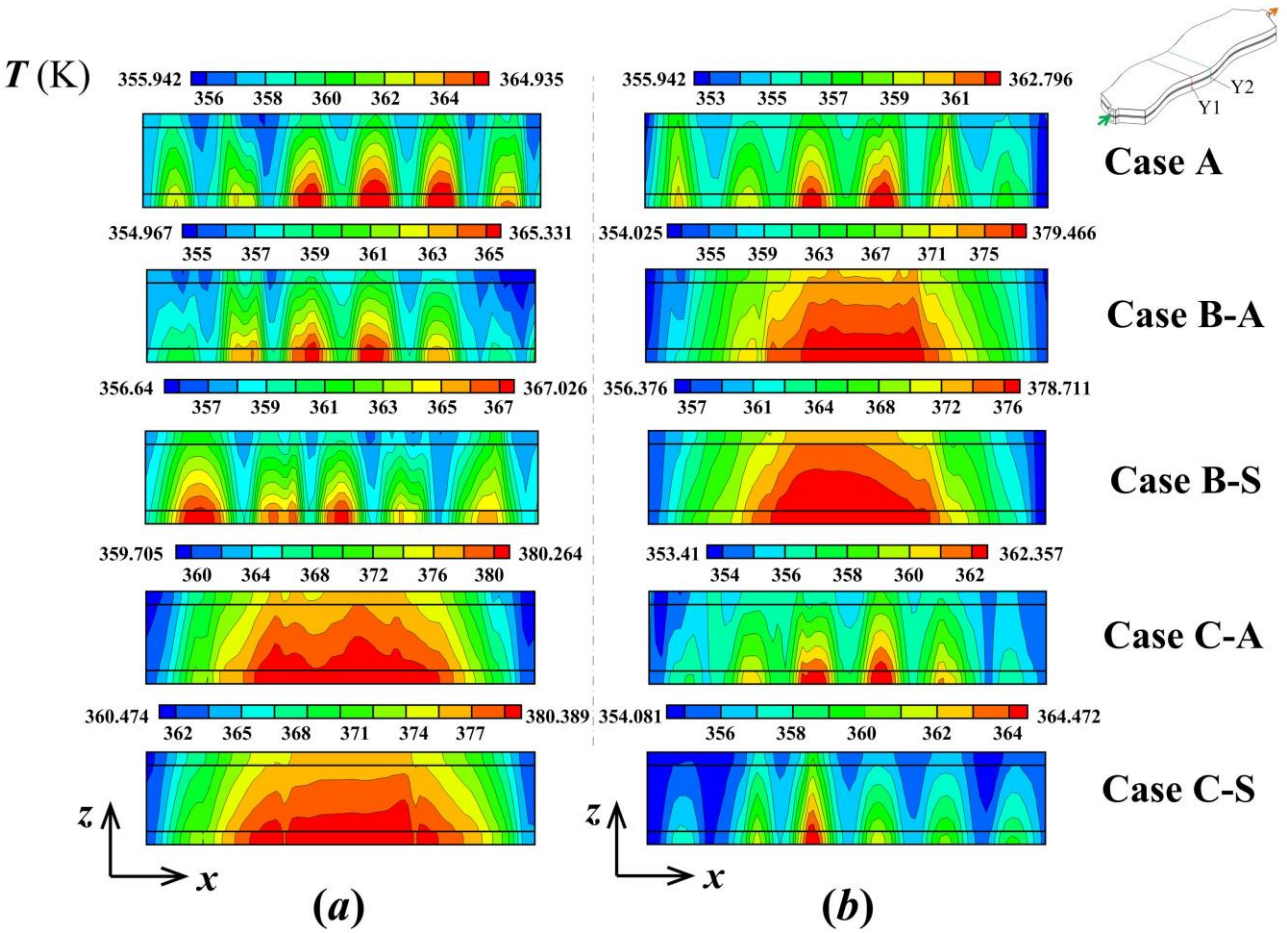

Fig.9 The temperature distribution of CL and membrane on Y1 and Y2 along the flow direction at 0.4V. (*a*) the temperature distribution on Y1; (*b*) the temperature distribution on Y2.

The local temperature distribution of the two discrete position (Plane Y1 and Y2) is shown in Fig.9. The temperature distribution of the novel structure is generally higher than that of Case A. Higher temperature regions occur at the cathode due to electrochemical process. And the temperature below the channels is higher than below the ribs. For Y1 (as shown in Fig. 9 (a)), the temperature distribution of the novel structure is different from that of Case A. The higher temperature region of Case C-A and Case C-S is greater than that of other cases, because the position is the discrete position of the two. The flow field, oxygen distribution and electrochemical rate were changed after the discrete. The temperature distribution is similar to Case A for the Case B-A and Case B-S, but the higher temperature region is slightly increased, especially Case B-S. For Y2 (as shown in Fig. 9 (b)), the distribution of higher temperature region is different to compared to

Y1. The higher temperature regions of Case B-A and Case B-S are greater than Case C-A and Case C-S, But the temperature distribution of Case C-A and Case C-S is similar to Case A. And the higher temperature region of Case C-S is smaller than Case A.

4.4 Oxygen distribution

The oxygen mass fraction distribution at the interface between the CL and GDL on cathode is shown in Fig. 10. The oxygen content decreases along the flow direction and the oxygen-rich regions are mainly in the middle and upstream. The oxygen concentration below the channels is higher than below the ribs, which is consistent with the temperature distribution because more oxygen is involved in the electrochemical reaction so that more heat being generated. Generally, the mass fraction of O_2 of Case A decreases gradually along the flow direction, while the novel structure has a local increase of oxygen in the discrete position. It can be seen from Fig. 9 that the higher temperature region of discrete position promotes the mass transfer, and the increase of O_2 can increase the temperature. Besides, the converged structure of the leading edge can increase the speed of the fluid itself, which can allow more oxygen to travel over longer distances in channel. Meanwhile, the oxygen distribution region in the middle and upstream of Case B-A and Case B-S is slightly larger than that of Case C-A and Case C-S.

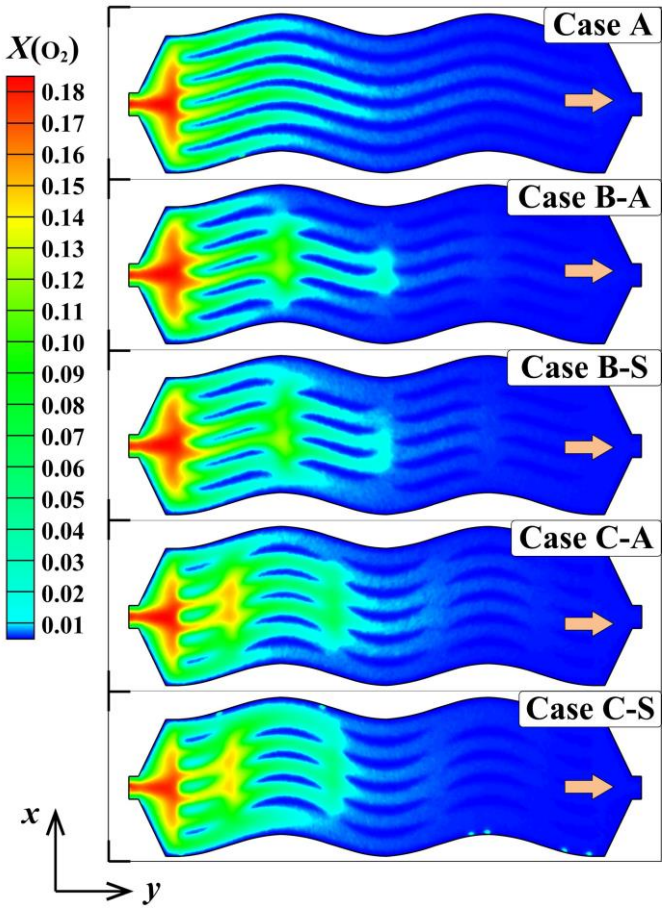

Fig.10 The mass fraction of O_2 at the interface between gas diffusion layer and catalyst layer on cathode at 0.4V.

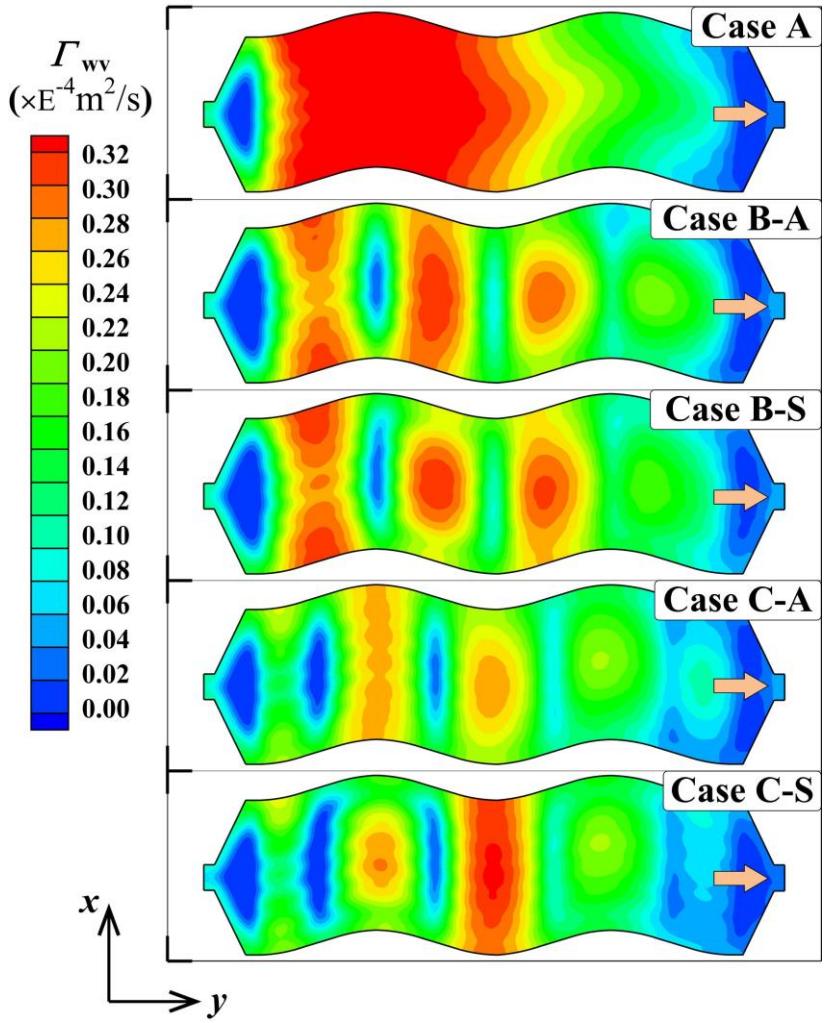

Fig.11 The diffusion coefficient of saturation water at the interface between gas diffusion layer and catalyst layer on cathode at 0.4V

4.5 Distribution and transfer properties of products

The diffusion coefficient of saturation water is shown in Fig. 11. The coefficient increases first along the flow channel and then decreases gradually for Case A. For the other novel structure, the overall trend also decreases along the flow direction. However, the local minimum values appear in the discrete position, which is obvious in Fig. 11. In PEMFC, there are three models of mass transfer: Electromigration under the action of an electric field at the electrolyte; The convective effect caused by the relative flow of solution; Diffusion by spontaneous movement of components under a concentration gradient. The mass transfer in PEMFC is not any one of the three modes. In order to maintain the dynamic balance in the whole transport process, the convection and diffusion must be adjusted each other. For the diffusion coefficient of saturation water, the change of velocity field will affect the distribution. It can be seen from Fig. 7 that the distribution of flow field and the change of velocity at the discrete points, which can promote the convective effect and diffusion transfer due to concentration gradient will be changed in Case A. In other word, the diffusion coefficient of saturation water of other cases decreases compared to Case A, especially at the discrete position. The flow field velocity of the novel structure is significantly improved compared

with Case A, which will facilitate the timely transfer of the generated water based on the greater flow field.

4.6 The pressure drop and electrochemical efficiency

Fig. 12 illustrates the pressure drop and electrochemical efficiency. It can be seen from the pressure drop of five cases that the pressure drop of the novel structure is less than the sinusoidal flow field (Case A). At the same time, the staggered flow field (Case B-S and Case C-S) has lower pressure drop. The pressure drop from high to low is: Case A > Case B-A > Case C-A > Case B-S > Case C-S. The lower pressure drop can indicate that the less energy is consumed to overcome the energy loss due to the pressure drop. For the electrochemical efficiency, the efficiency improvement are: 21.07% (Case B-A), 23.61% (Case B-S), 22.15% (Case C-A) and 6.97% (Case C-S) compared with Case A. The electrochemical efficiency improvement of the novel structure is most obvious in Case B-S, which means that the chemical energy utilization rate of fuel is higher.

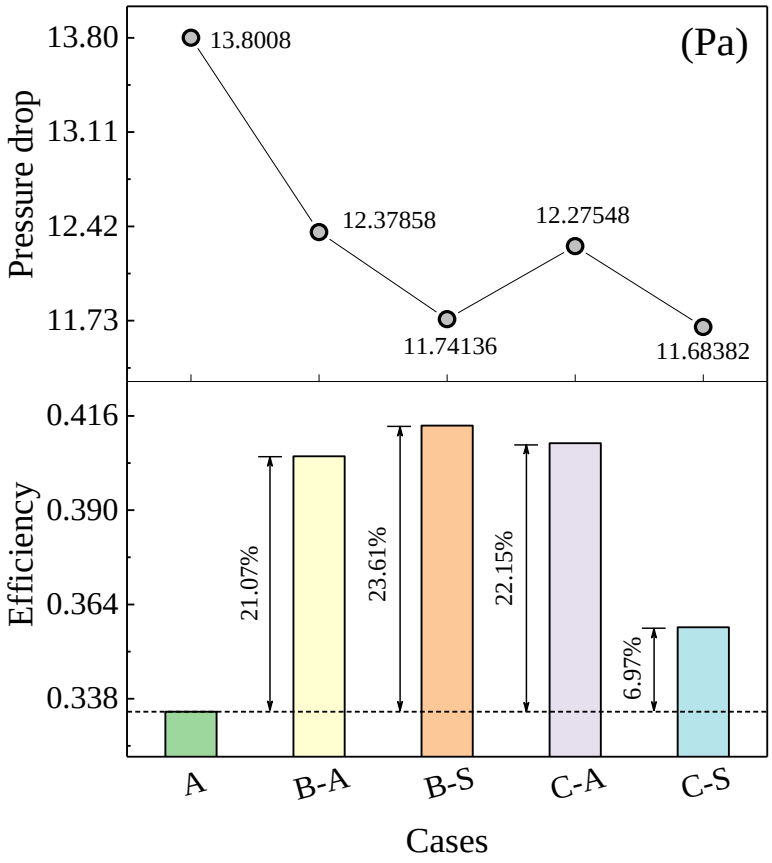

Fig.12 The pressure drop and electrochemical efficiency of the PEMFC.

5. SUMMARY AND CONCLUSIONS

In the paper, the performance of PEMFC with a novel flow field structure based on the discontinuous S-shaped and crescent ribs are investigated and discussed. The flow, mass transfer, temperature and pressure drop are analyzed. According to the above discussed, these two novel flow field have better performance compared with sinusoidal flow field (Case A). Meanwhile, some valuable conclusions are drawn as follows.

1) The output performance of the discontinuous S-shaped and crescent ribs flow fields are better than sinusoidal. The performance of PEMFC is different from the flow pattern in discrete location. The electrochemical efficiency of PEM fuel cell will be improved based on two novel flow fields, among which the discontinuous S-shaped ribs flow field (Case B-S) has the best performance and the efficiency can be improved by 23.61% in the case of stagger in high current density

2) Two novel structures can improve the flow pattern of sinusoidal flow field, especially at flow turning points. Lower-speed zones at flow turning points are avoided (i.e. the velocity is improved) and are conducive to the transport of mass, especially water. The improvement of flow field is most obvious in Case B-A and Case B-S.

3) At the interface between CL and GDL on cathode, the oxygen-rich area on the same activation area increases at the discrete position, which leading to the accelerated electrochemical rate and the production of more heat. And the diffusion coefficient of water saturation will decrease under the local convection effect in the discrete region.

4) The local temperature of the novel floe field was higher than of the sinusoidal flow field at different discrete positions because more oxygen enrichment led to the increase in electrochemical rate. And the mean temperature of the membrane as a whole increases. Although the temperature uniformity of the novel flow field is worse than that of the sinusoidal flow field (Case A), the uniformity index fluctuates between 0.9930 – 0.9955.

5) The pressure drop of the novel flow fields is lower than that of the sinusoidal flow field (Case A), which indicates that the two novel flow field have less energy consumption. It is worth noting that the stagger structure has a lower pressure drop for the two novel flow field.

ACKNOWLEDGEMENTS

This work was sponsored by the National 111 Project under Grant no. B18041. Prof. Meng Ni would thank the grant (Project Number: PolyU 152214/17E) from Research Grant Council, University Grants Committee, Hong Kong SAR.

REFERENCES

[1] Abe JO, Popoola API, Ajenifuja E, Popoola OM. Hydrogen energy, economy and storage: Review and recommendation. *International Journal of Hydrogen Energy* 2019;44:15072-15086.

[2] Garche J, Jörissen L. *Handbook of Fuel Cells – Fundamentals, Technology and Applications*. New York: Wiley; 2010.

[3] Eikerling M, Kulikovsky A. *Polymer Electrolyte Fuel Cells: Physical Principle of materials and Operation*. New York: CRC Press; 2014.

[4] Huo S, Jiao K, Park JW. On the water transport behavior and phase transition mechanisms in cold start operation of PEM fuel cell. *Applied Energy* 2019;233-234:776-788.

[5] Roudgar A, Narasimachary SP, Eikerling M. Ab initio study of surface medicated proton transfer in polymer electrolyte membranes. *Chem. Phys. Lett* 2008;457(4):337-341.

[6] Arntsen C, Savege J, Tse YLS, Voth GA. Simulation of proton transport in proton exchange membranes with reactive molecular dynamics. *Fuel Cell* 2016;6:695-703.

[7] Darcy C, Anusorn K, Jacob J. Proton conduction and oxygen diffusion in ultra-thin Nafion films in PEM Fuel Cell: How thin?. *Journal of the Electrochemical Society* 2019;166(2):F24-F33.

[8] Qiao M, Titirici MM. Engineering the interface of carbon electrocatalysts at the triple point for enhanced Oxygen Reduction Reaction. *Chemistry-A European Journal* 2018;24:18374-18384.

[9] Yang XH, Wang YC, Zhang GX, Du L, Yang LJ, Markiewicz M, Choi J, Chenitz R, Sun SH. SiO_2-Fe/N/C catalyst with enhanced mass transport in PEM fuel cells. *Applied Catalysis B: Environmental* 2020;264:118523.

[10] Harvey D, Pharoah JG, Karan K. A comparison of different approaches to modelling the PEMFC catalyst layer. *Journal of Power Sources* 2008;179:209-219.

[11] Xie B, Zhang GB, Xuan J, Jiao K. Three-dimensional multi-phase model of PEM fuel cell coupled with improved agglomerate sub-model of catalyst layer. *Energy Conversion and Management* 2019;199:112051.

[12] Hou YZ, Deng H, Nada Z, Du Q, Jiao K. 3D lattice Boltzmann modeling of droplet motion in PEM fuel cell channel with realistic GDL microstructure and fluid properties. *International Journal of Hydrogen Energy* 2020;45:12476-12488.

[13] Chen T, Liu SH, Zhang JW, Tang MN. Study on the characteristics of GDL with different PTFE content and its effect on the performance of PEMFC. *International Journal of Heat and Mass Transfer* 2019;128:1168-1174.

[14] Alhazmi N, Ingham DB, Ismail MS, Hughes KJ, Ma L, Pourkashanian M. Effect of the anisotropic thermal conductivity of GDL on the performance of PEM fuel cell. *International Journal of Hydrogen Energy* 2013;38:603-611.

[15] Li SA, Yuan JL, Andersson M, Xie GN, Sundén B M. Influence of anisotropic das diffusion layers on transport phenomena in a proton exchange membrane fuel cell. *International Journal of Energy Research* 2017;41:2034-2050.

[16] Gundlapalli R, Jayanti S. Performance characteristics of several variants of interdigitated flow fields for flow battery applications. *Journal of Power Sources* 2020;467:228225.

[17] Vijayakrishnan MK, Palaniswamy K, Ramasamy J, Kumaresan T, Manoharan K, Rajagopal TKR, Maiyalagan T, Jothi VR, Yi SC. Numerical and experimental investigation on 25 cm^2

and 100 cm^2 PEMFC with novel sinuous flow field for effective water removal and enhanced performance. *International Journal of Hydrogen Energy* 2020;45:7848-7862.

[18] Ozden A, Ercelik M, Ouellette D, Colpan CO, Ganjehsarabi H, Hamdullahpur F. Designing, modeling and performance investigation of bio-inspired flow field based DMFCs. *International Journal of Hydrogen Energy* 2017;42:21546-21558.

[19] Atyabi SA, Afshari E. A numerical multiphase CFD simulation for PEMFC with parallel sinusoidal flow fields. *Journal of Thermal Analysis and Calorimetry* 2019;135:1823-1833.

[20] Anyanwu IS, Hou YZ, Xi FQ, Wang XY, Yin Y, Du Q, Jiao K. Comparative analysis of two-phase flow in sinusoidal channel of different geometric configurations with application to PEMFC. *International Journal of Hydrogen Energy* 2019;44:13807-13819.

[21] Wilberforce T, El-Hassan Z, Ogungbemi E, Ijaodola O, Khatib FN, Durrant A, Thompson J, Baroutaji A, Olabi AG. A comprehensive study of the effect of bipolar plate (BP) geometry design on the performance of proton exchange membrane (PEM) fuel cells. *Renewable and Sustainable Energy Reviews* 2019;111:236-260.

[22] Wang BW, Chen WM, Pan FW, Wu SY, Zhang GB, Park JW, Xie B, Yin Y, Jiao K. A dot matrix and sloping baffle cathode flow field of proton exchange membrane fuel cell. *Journal of Power Sources* 2019;434:226741.

[23] Atyabi SA, Afshari E. Three-dimensional multiphase models of proton exchange membrane fuel cell with honeycomb flow field at the cathode side. *Journal of Cleaner Production* 2019;214:738-748.

[24] Chen T, Xiao Y, Chen TZ. The impact on PEMFC of bionic flow field with a different branch. *Energy Procedia* 2012;28:134-139.

[25] Wen ZX, Lv YG, Li Q. Comparative study on flow and heat transfer characteristics of sinusoidal and zigzag channel printed circuit heat exchangers. *Science China Technological Sciences* 2020;63(4):655-667.

[26] Nilpueng K, Ahn HS, Jerng DW, Wongwises S. Heat transfer and flow characteristics of sinusoidal wavy plate fin heat sink with and without crosscut flow control. *International Journal of Heat and Mass Transfer* 2019;137:565-572.

[27] Tsuzuki N, Kato Y, Nikitin K, Ishizuka T. Advanced microchannel heat exchanger with S-shaped fins. *Journal of Nuclear Science and Technology* 2009;46(5):403-412.

[28] Ngo TL, Kato Y, Nikitin K, Tsuzuki N. New printed circuit heat exchanger with S-shaped fins for hot water supplier. *Experimental Thermal and Fluid Science* 2006;30:811-819.

[29] Alawadhi K, A.Alnaqi A, Murad AE, A.M.Husain E. Thermal and hydraulic performance of an SCO2 printed circuit heat exchanger(PCHE) with new channel geometry based on a cosine curve. *International Journal of Applied Engineering Research* 2019;14(14):3231-3241.

[30] Dong PC, Xie GN, Ni M. The mass transfer characteristics and energy improvement with various partially blocked flow channel in a PEM fuel cell. *Energy* 2020;206:117977.

[31] Qiu DK, Peng LF, Tang JY, Lai XM. Numerical analysis of air-cooled polymer electrolyte membrane fuel cells with various cathode flow channels. *Energy* 2020;198:117334.

[32] Tijani AS, Ghani MFA, Rahim AHA, Muritala IK, Mazlan FAB. Electrochemical characteristics of (PEM) electrolyzer under influence of charge transfer coefficient. *International Journal of Hydrogen Energy* 2019;44:27177-27189.

[33] Barbir F. *PEM Fuel Cells: Theory and Practice, second edition.* New York: Elsevier; 2013.

[34] Buchanan F. *PEM Fuel Cell: Theory, Performance and Application* . New York: Nova Science Publishers; 2015.

[35] Wu H, Li XG, Berg P. On the modeling of water transport in polymer electrolyte membrane fuel cells. *Electrochimica Acta* 2009;54:6913-6927.

[36] Al-Baghdadi MARS. Three-dimensional computational fluid dynamics model of a tubular-shaped PEM fuel cell. *Renewable Energy* 2008; 33:1334-1345.

[37] Wang L, Husar A, Zhou TH, Liu HT. A parametric study of PEM fuel cell performance. *International Journal of Hydrogen Energy* 2003; 28:1263-1272.

Table 1 Computational domain design parameters and working condition

Parameters	Parameters explanation	Value	Unit
W	The width of computational domain	12	mm
H	The total height of computational domain	3.47	mm
L	The length of the channel	50	mm
H_{CC}	The height of current collector	1.5	mm
H_{CH}	The height of inlet/outlet	1.0	mm
H_{gdl}	The thickness of gas diffusion layer	0.2	mm
H_{cl}	The thickness of catalyst layer	0.01	mm
H_{mem}	The thickness of membrane	0.05	mm
W_{CH}	The width of inlet/outlet	1.0	mm
α	The inlet and outlet angle	120°	-
θ	The bend angle	10°	-
p	The cell operating pressure	3.0	atm
T	The cell operating pressure	353.15	K
RH_a /RH_c	Relative humidification in anode/cathode	100%/100%	-
ζ_a /ζ_c	Stoichiometry ratio in anode/cathode	1.0/1.0	-

Table 2 The source term of conservation equations

Source term	Explanation	Expression	Zone
S_{mass}	The source term of the mass conservation	$S_{mass} = S_{H_2} + S_{O_2} + S_{H_2O}$	Anode: CL and GDL Cathode: CL and GDL
$S_{\vec{u}}$	The source term of the momentum conservation	$S_{\vec{u}} = -\frac{\mu}{K}\vec{u}$	Anode: CL and GDL Cathode: CL and GDL
S_T	The source term of the energy conservation	$S_T = \left(\frac{\vec{i}_e^{\,2}}{k_e^{eff}} + \frac{\vec{i}_s^{\,2}}{\sigma_s^{eff}}\right) + j\left(\eta + T\frac{dU_0}{dT}\right) + h_L$	Membrane: Anode: CL and GDL Cathode: CL and GDL
S_{H_2}	The species source term of H_2	$S_{H_2} = -\frac{M_{H_2}}{2F} i_a$	Anode: CL
S_{O_2}	The species source term of O_2	$S_{O_2} = -\frac{M_{O_2}}{4F} i_c$	Cathode: CL
S_{H_2O}	The species source term of H_2O	$S_{O_2} = \frac{M_{H_2O}}{2F} i_c$	Anode: CL Cathode: CL
S_{ϕ_p}	The proton conservation equation	$S_{\phi_p} = +i_a$ or $S_{\phi_p} = -i_c$	Anode: CL ($S_{\phi_p} = +i_a$) Cathode: CL ($S_{\phi_p} = -i_c$)
S_{ϕ_e}	The electron conservation equation	$S_{\phi_e} = -i_a$ or $S_{\phi_e} = +i_c$	Anode: CL ($S_{\phi_e} = -i_a$) Cathode: CL ($S_{\phi_e} = +i_c$)

Table 3 The physical parameters and material characteristic parameters

Item	Explanation	Value	Unit
E_{OCV}	Open circuit voltage	0.95	V
C_a^{ref} / C_c^{ref}	Ref. concentration in anode/cathode	546.5/3.39	mol/m^3
$i_a^{ref} \times a$ / $i_c^{ref} \times a$	Ref. exchange current density in anode/cathode	1.0×10^9/2.5×10^3	A/m^3
EW	Equivalent weight of membrane	1.1	kg/mol
θ_c	Contact angle	120°	-
D_i^0	Ref. diffusivity of H_2/O_2/H_2O	9.15×10^{-5}/2.2×10^{-5}/2.56×10^{-5}	m^2/s
ρ	Density of membrane/CL/GDL	1980/2719/2719	kg/m^3
ε	Porosity of CL and GDL	0.5	-
c_p	Specific heat of membrane/CL/GDL/CC	2000/871/871/871	J/kg·K
k_{eff}	Thermal conductivity of membrane/CL/CC	0.25/0.3/100	W/kg·K
$k_{gdl,x}$ / $k_{gdl,z}$	Thermal conductivity of GDL	1.7/21	W/kg·K
κ_e	Electrical conductivity of CL/GDL/CC	2000/5000/20000	1/ohm·m